



Article

Broadband achromatic metalens in terahertz regime

Qingqing Cheng^{a,*}, Meilin Ma^a, Dong Yu^a, Zhixiong Shen^b, Jingya Xie^a, Juncheng Wang^a, Nianxi Xu^c, Hanming Guo^a, Wei Hu^b, Shuming Wang^{b,*}, Tao Li^{b,*}, Songlin Zhuang^{a,*}

^a Shanghai Key Lab of Modern Optical System and Engineering Research Center of Optical Instrument and System (Ministry of Education), University of Shanghai for Science and Technology, Shanghai 200093, China

^b National Laboratory of Solid State Microstructures, College of Engineering and Applied Sciences, School of Physics, Nanjing University, Nanjing 210093, China

^c Changchun Institute of Optics, Fine Mechanics and Physics, Chinese Academy of Sciences, Changchun 130033, China

ARTICLE INFO

Article history:

Received 11 May 2019

Received in revised form 12 July 2019

Accepted 25 July 2019

Available online 9 August 2019

Keywords:

Far infrared or terahertz

Achromatic

Metasurface

Diffraction theory

ABSTRACT

Achromatic focusing is essential for broadband operation, which has recently been realised from visible to infrared wavelengths using a metasurface. Similarly, multi-terahertz functional devices can be encoded in a desired metasurface phase profile. However, metalenses suffer from larger chromatic aberrations because of the intrinsic dispersion of each unit element. Here, we propose an achromatic metalens with C-shaped unit elements working from 0.3 to 0.8 THz with a bandwidth of approximately 91% over the centre frequency. The designed metalens possesses a high working efficiency of more than 68% at the peak and a relatively high numerical aperture of 0.385. We further demonstrate the robustness of our C-shaped metalens, considering lateral shape deformations and deviations in the etching depth. Our metalens design opens an avenue for future applications of terahertz meta-devices in spectroscopy, time-of-flight tomography and hyperspectral imaging systems.

© 2019 Science China Press. Published by Elsevier B.V. and Science China Press. All rights reserved.

1. Introduction

Conventional focused terahertz components, such as spherical single convex lenses or off-axial parabolic mirrors [1], are generally bulky, costly and time-consuming to manufacture with high precision. Furthermore, these terahertz instruments based on the bulky components still have several limitations, which either solely function at specific frequencies or bring significant difficulties to the design and construction of the terahertz system [2]. Compared to conventional bulky footprint devices realizing phase modulation through optical path accumulation, metasurface lenses [3,4] or “metalenses” introduce an abrupt modulation of light wavefronts in two-dimensional (2D) space, composed of arrays of metallic or dielectric micro/nano-scatterers [3–6]. The rapid advancements in metasurfaces have led to considerable research on many novel photonic devices [7–13] and phenomena such as wave deflection [10–13], focusing [14–16] and imaging [17–19]. However, these proposed metasurface functions still pose the challenges of large chromatic aberrations and considerable losses [9,20]. In addition, few experimental works have been reported on efficient terahertz

achromatic meta-devices based on all-dielectric metasurfaces [21–23].

Most imaging systems suffer from chromatic aberrations, because incident light with a continuous wavelength generates numerous focal spots at different spatial locations. For metasurface devices, chromatic aberration correction can be achieved by the careful design of complementary structures and contribute to high-performance imaging systems [24–30]. To date, several pioneering investigations for dispersion engineering and optimization algorithms [18,31–33] have been proposed to eliminate chromatic dispersions. For instance, Wang et al. [34] employed complex metallic unit elements with smooth and linear phase dispersions as well as geometric phases to design a broadband achromatic flat metalens with numerical aperture $NA = 0.268$. Recently, Chen et al. [35] proposed an achromatic metalens with $NA = 0.2$ by separately engineering the group delay and group delay dispersion of each constituent nanostructure, which are independent of its phase. Wang et al. [36] also demonstrated full-colour imaging of an achromatic metalens with $NA = 0.106$ by integrated resonances for the required phase compensation. The important aforementioned progress of metalenses was shown to be capable of achromatic imaging by tailoring the phase dispersion of each nanostructure. Most of the studies have focused on meta-devices in the visible or near-infrared region [37,38]. However, investigations of achromatic metalenses using dielectric

* Corresponding authors.

E-mail addresses: qqcheng@usst.edu.cn (Q. Cheng), wangshuming@nju.edu.cn (S. Wang), taoli@nju.edu.cn (T. Li), slzhuang@yahoo.com (S. Zhuang).

metasurfaces have seldom been reported in the terahertz regime possessing a high working efficiency. In addition, all the achromatic metalenses have a small NA, owing to the limited phase shift coverage of resonant units, which also limits the design. Therefore, it is still challenging to design an achromatic metalens that can eliminate the chromatic effect over a broad band of wavelengths in the terahertz region.

Here, in order to address these challenges from traditional terahertz lenses, we first demonstrate an ultra-broadband achromatic terahertz metalens that operates within 0.3–0.8 THz at about 91% of the central frequency. Based on terahertz near-field microscopy, the phase of the electric field component transmitted by the metalens coincides with the phase of the theoretical design. Owing to the extremely large etching aspect ratio of 1:25, we achieve a large phase compensation from the metalens unit elements, which enables us to simultaneously obtain a relatively high NA value, $NA = 0.385$, and a large metalens diameter, $D = 10$ mm. Moreover, the C-shaped unit elements we employed in this work exhibit a more robust phase accumulation than the usual rectangular structures. The metalens is fabricated on a silicon substrate with a thickness of only several hundred microns, which is quite desirable for integration and miniaturization. Our work significantly promotes the development of achromatic meta-devices in terahertz hyperspectral imaging and can be used to investigate the robustness of metasurface functional designs.

2. Theoretical realizations of broadband achromatic metalens

As shown in the schematic in Fig. 1a, the proposed terahertz achromatic metalens is composed of silicon pillars arranged on a square lattice. The required phase distribution for each unit element at the position (x, y) satisfies the following equation:

$$\varphi(x, y) = -2\pi \left(\sqrt{x^2 + y^2 + F^2} - F \right) \frac{1}{\lambda}, \quad (1)$$

where λ represents the wavelength of the input wave and F is the focal length. The input plane wave is modulated into a converging wavefront through the elements. In order to clarify a terahertz broadband achromatic metalens, a fixed focal length is exactly maintained in a wide wavelength range. It can be found from Eq. (1) that the phase compensation should follow a linear relation with $1/\lambda$ (or frequency) in a continuous terahertz frequency range. Generally, for the case of the working wavelength range $\lambda \in \{\lambda_{\min}, \lambda_{\max}\}$, where λ_{\min} (or f_{\max}) and λ_{\max} (or f_{\min}) are the boundaries of the

working wavelength range, the designed phase distribution can be divided into two components:

$$\varphi_1(x, y) = -2\pi \left(\sqrt{x^2 + y^2 + F^2} - F \right) \frac{1}{\lambda_{\max}}, \quad (2)$$

$$\begin{aligned} \varphi_2(x, y) &= \varphi(x, y) - \varphi_1(x, y) \\ &= -2\pi \left(\sqrt{x^2 + y^2 + F^2} - F \right) \left[\frac{1}{\lambda} - \frac{1}{\lambda_{\max}} \right], \end{aligned} \quad (3)$$

where the former $\varphi_1(x, y)$ in Eq. (2) is considered as a basic phase profile, which is solely related to λ_{\max} and independent of the working wavelength λ . Such a phase profile can be acquired by exploiting the geometric phase, which only depends on the orientation of the unit elements. The latter $\varphi_2(x, y)$ in Eq. (3) is a function of the working wavelength and presents a linear relation with $1/\lambda$, which is considered as the phase difference induced from various incident wavelengths. Such phase differences can be obtained by suitably designing the phase of each resonance unit of the metalens, which must also exhibit a phase dispersion with a linear relation with $1/\lambda$ such as $\varphi_2(x, y)$. As the mechanism of the resonant phase is completely different from the geometric phase, these two phase shapes will not disturb each other and can be simply merged together. An additional phase shift $\Delta\varphi$ should be introduced to realise the phase compensation effect from the specially designed metalens, as shown in Fig. 1b.

The method by which to tailor the resonance phase by adjusting the structural parameters is critical for broadband terahertz achromatic focusing. Here, the working frequency is chosen in the terahertz regime, that is, $\{f_{\min}, f_{\max}\} \rightarrow \{0.3 \text{ THz}, 0.8 \text{ THz}\}$ or $\{\lambda_{\min}, \lambda_{\max}\} \rightarrow \{375 \mu\text{m}, 1,000 \mu\text{m}\}$. In our design, the basic unit element of the metalens contains solid and inverse high-resistance silicon nanostructures, from which we implement the phase compensation by carefully setting various parameters of the C-shaped unit elements. The unit elements contain the inner diameter, outer diameter and opening angle (or the rectangular unit elements have the parameters of length and width) at different specific positions. In addition, the basis phase distribution of the dielectric metasurface for focusing can be satisfied by rotating each unit element. Consequently, the achromatic focusing properties can be implemented simultaneously on a single-layer structure array.

The simulations are performed using the Lumerical FDTD software with a right circularly polarised (RCP) plane wave illuminated from the substrate and periodic boundary conditions set at the boundaries of the simulation domains for these two basic unit element shapes. Fig. 2a and b show the simulated amplitudes and

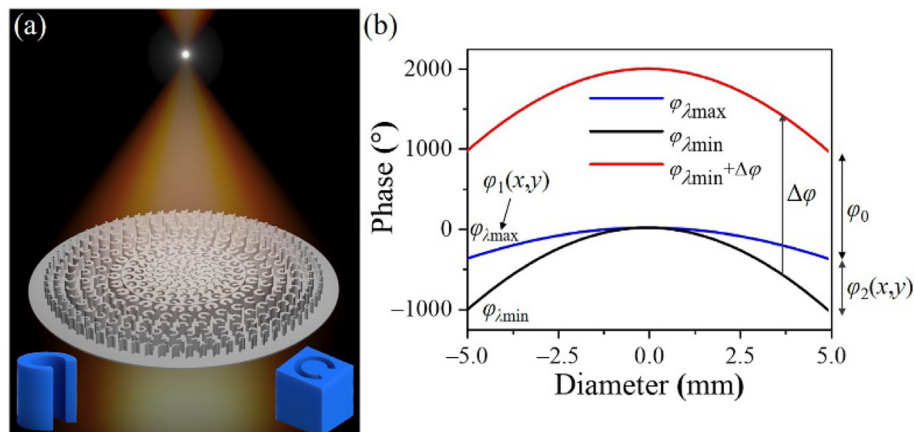


Fig. 1. (Color online) Schematic of achromatic metalens. (a) Schematic of C-shaped (or rectangular) unit element-based achromatic metalens. (b) Phase profile for achromatic metalens at the wavelength range of $\lambda \in \{\lambda_{\min}, \lambda_{\max}\}$, where $\Delta\varphi$ is a certain positive value.

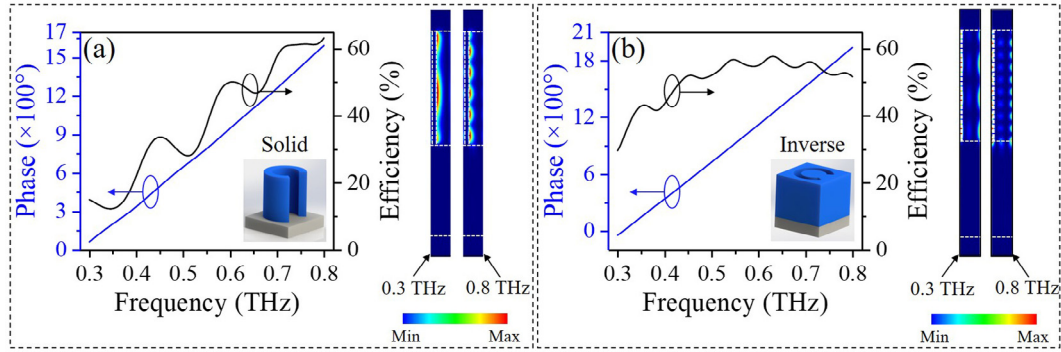


Fig. 2. (Color online) Phase distributions and conversion efficiencies of the solid and inverse C-shaped unit element. RCP-to-LCP polarization conversion efficiency (black curves) and phase profile (blue curves) of the (a) solid and (b) inverse C-shaped unit element. Side views of normalised magnetic density distributions in each typical unit at 0.3 THz (left) and 0.8 THz (right) on the right side of (a) and (b).

phase distributions of the solid and inverse C-shaped unit element as a function of the terahertz frequency (f) with a lattice constant $p = 100 \mu\text{m}$. By varying the structural parameters, the linear phase coverage can achieve multiples of 2π in the working frequency range from 0.3 to 0.8 THz. The phase realization mechanism originates from the waveguiding effect. The phase is given by $n_{\text{eff}} \cdot h \cdot 2\pi / \lambda$ [18], where n_{eff} and h (structural height) are the effective index of the waveguide mode and the propagation length, respectively. Based on the waveguide model, the effective refractive index increases with the frequency, which is the reason for the greater phase changes with the frequency. The side views of the normalised magnetic densities in a periodic unit at frequencies of 0.3 and 0.8 THz are shown on the right side of Fig. 2a and b. The amplitude and the phase details of the rectangular unit elements are shown in Fig. S1 (online). More details for these two structures can be found in Tables S1–S4 (online). Clearly, the field distributions of the inverse structures in the vertical cross-section present more wave nodes than those of the solid structures, which indicate that the inverse structures have larger compensation phases compared to the solid ones. The electromagnetic field coupling effects between neighbouring units can be ignored, so the phase design for each unit is still accurate when they are arranged in a square lattice of the unit array.

3. Experimental characterizations of the achromatic metalens

To verify our proposed approaches, we fabricate the terahertz achromatic metalens to focus the terahertz wave and explore the corresponding behaviour using terahertz near-field microscopy, as shown in Fig. 3a. The sample shown in Fig. 3b is fabricated by conventional photolithography and deep etching processing techniques. Scanning electron microscope (SEM) images of the C-shaped sample are shown in Fig. 3c and d. Fig. 3c represents the inverse C-shaped unit elements in the inner area of the metalens, while Fig. 3d shows the solid C-shaped unit elements in the margin area. The inner inverse structures provide a higher compensation phase than the margin solid structures, which are consistent with the phase distribution, as shown in Fig. 1b. The solid structures with a height of $550 \mu\text{m}$ are etched into the silicon substrate with a thickness of 1 mm, and the refractive index is $n = 3.45$ (resistivity $> 10^4 \Omega\text{-cm}$). The experimental setup is illustrated in Fig. 3a, and the collimated terahertz waves radiate from a 100-fs ($\lambda = 780 \text{ nm}$) laser pulse-pumped photoconductive antenna emitter, are modulated with a proper polarised state, and then impinge on the sample. To enable a three-dimensional scan of the terahertz electric field in the x - y plane, a commercial terahertz near-field probe is mounted on a three-dimensional motorised stage. The

sample is also mounted on a three-dimensional translation stage. The probe is located in the vicinity of ($\sim 3 \text{ mm}$) the sample to collect the signals to reconstruct the amplitudes and phase distributions of the electric field. Here, a microscope is used to identify the distance between the probe and the metasurface. The 2D motorised field distribution is detected with a discrete step size of 0.25 mm in the x - and y -directions.

By employing the above-proposed design principle, a broadband achromatic metalens is demonstrated in a broadband terahertz frequency range from 0.3 to 0.8 THz. A metalens composed of C-shaped unit elements with $\text{NA} = 0.385$ is obtained with a diameter of 10 mm and focal length of 12 mm. The transmitted field intensity profiles of the horizontal polarization (E_y) on the transverse focal plane are shown in Fig. 4a–c. The measured results are highly consistent with the simulation, as shown in Fig. 4g–i, which indicate that the focal length of $F = 12 \text{ mm}$ remains almost unchanged in the broadband frequency range. The achromatic metalens focusing at the frequencies of 0.3, 0.6 and 0.8 THz is supported by the detected phase distributions, which are shown in Figs. S3 and S4 (online). Furthermore, additional information of the experiments for the metalens based on C-shaped unit elements are shown in Figs. S5 and S6 (online). In order to visually demonstrate the superiority of the achromatic metalens, we simulated the chromatic aberration effect of ordinary lenses in Fig. S2 (online). All the measured focal spots show values of the full-width at half-maximum (FWHM) close to the diffraction-limited size of $\lambda / (2\text{NA})$, as shown in Fig. 4d–f. For example, Fig. 4d shows the horizontal intensity profile at the focal spot for the experimental and numerical results at the terahertz frequency of 0.3 THz with the corresponding wavelength of 1 mm. The theoretical diffraction-limited value of $\lambda / (2\text{NA})$ is 1.298 mm, which is quite close to the experimental value of 1.3 mm. Similarly, the measured numerical apertures from the experimental results at the frequencies of 0.6 and 0.8 THz are also $\text{NA} = 0.385$, which match the designed value perfectly. These results prove that achromatic focusing has been realised in such a terahertz broadband.

The experimental efficiency of the C-shaped metalens at the incident wavelength at 0.6 THz is shown in Fig. 4j, in which the efficiency has been calculated using $\sum I_E / \sum (I_{\text{ref}} \times n_{\text{si}})$, where I_E represents the sum of the intensity distributions at the focal plane with a diameter 1.5 mm (dotted white line) and I_{ref} is the transmitted terahertz power with a silicon wafer. We have demonstrated a metalens with an efficiency higher than 68% at the peak, which is promoted significantly higher than the efficiency of the metalenses based on plasmonic scatterers and recent reports of dielectric achromatic metalenses. In all cases, the reasons for efficiency reduction in the achromatic metalens include amplitude variations (not all meta-units have the same scattering efficiency), phase

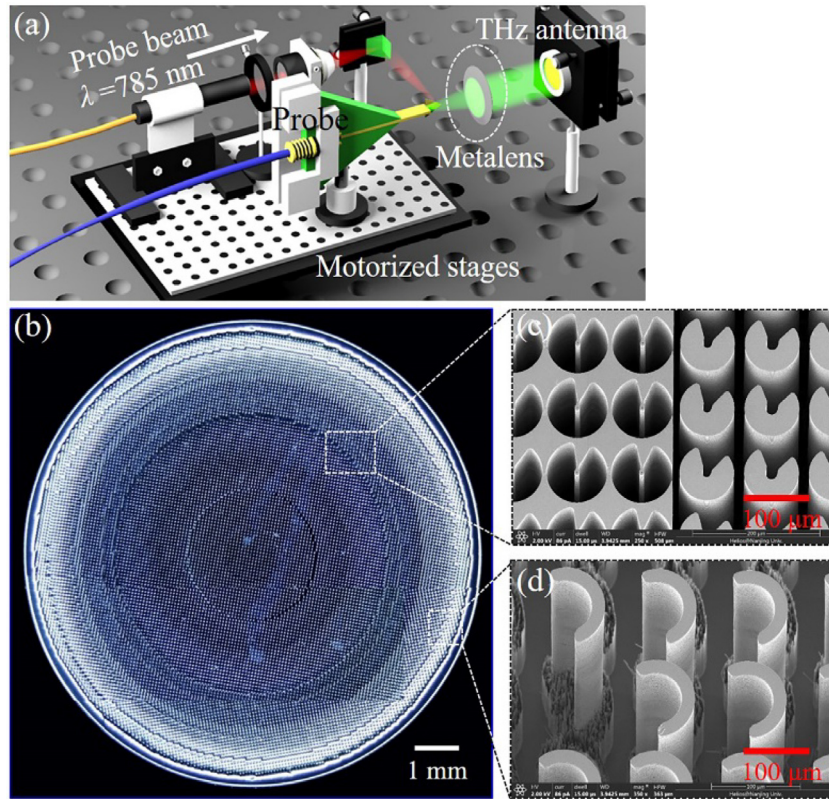


Fig. 3. (Color online) (a) Experimental setup of the terahertz near-field microscopy. The terahertz near-field probe is fixed on the motorised stage to detect the electric field distributions. (b) Top view of the fabricated sample with a diameter of 10 mm. (c) Enlarged view of the inverse and solid unit elements in the inner area of the metasurface. (d) Enlarged view of the solid C-shaped unit elements in the margin area of the metasurface.

errors due to the mismatch between the required and actual phase responses of the meta-units, and fabrication errors (such as side-wall roughness and slope). In our transmission mode metalens, backscattering from the meta-units sacrifices about 30% of the overall efficiency. In order to clearly present the overall efficiency, Fig. 4k–m also show the incident, LCP focusing and RCP defocusing distribution at the frequency of 0.6 THz, respectively.

4. Influences of fabrication defects

We found that the sensitivity of the focusing effects on the fabrication robustness for C- and rectangular unit-based metalenses is different. These two metalenses with different structural shapes are adjacently fabricated on a silicon wafer, ensuring that the lens has the same fabrication error. Fig. 5a shows SEM images of two typical structure units of the metalens, and the fabrication defects. These defects which include the shape deformations and deviations of etching depth inevitably make negative impacts on the focusing effects and broaden the FWHMs of the focal spots, as shown in Fig. 5b. The simulated FWHM is 0.6 mm at the frequency of 0.5 THz, compared to the experimental value of 1.05 mm. In order to deepen the understanding of the influences of the shape deformations, we numerically illustrated the phase profiles with the variation in the fillet errors, as shown in Fig. 5c and d. We found that the deviations in the actual and ideal phase distributions of the metalens based on the C-shaped unit are smaller than those based on the rectangular unit, which indicate that the metasurface based on the C-shaped unit is less affected by the fabrication defects. Fig. 5e also presents the focal spot of the metalens based on the rectangular unit at the frequency of 0.5 THz. The focal length in the experimental data is $F \approx 10.5$ mm, which has a small

offset from our designed value of $F = 10.5$ mm. The experimental results based on the amplitude and phase distributions of the rectangular metalens are presented in Figs. S5 and S6 (online). The simulation results of the focusing effect with C-shaped fillet errors are presented in Fig. S7 (online).

Furthermore, we compare the achromatic focusing distributions of various etching depths using simulations (Fig. 6). The greater the depth, the higher the compensation phase, which in turn achieves a broader achromatic bandwidth or larger numerical aperture. From the simulation results in Fig. 6a–c at the frequency of 0.3 THz, the focal length increases from 12 to 19 mm, which implies decreased numerical apertures when the unit element depth decreases from 550 to 350 μm . This is consistent with the above-mentioned relationship between the depth and resonant modes. In addition, the focal lengths in Fig. 6d–f at the frequency of 0.8 THz obey the same tendency. Fig. 6g summarises the profiles of Fig. 6d–f at the frequency of 0.8 THz with the etching depths of 550, 450 and 350 μm . Importantly, it is found that the focal lengths in Fig. 6a and d remain the same at the frequencies of 0.3 and 0.8 THz, which also demonstrate the achromatic effects within the wavelength range between these two frequencies. The same cases are shown in Fig. 6b, e and Fig. 6c, f, respectively, which again prove the robustness of the achromatic metalens. The transmitted field intensity profiles of the metalens with varied structural depths at various incident wavelengths are shown in Figs. S8 and S9 (online) for the C-shaped and the rectangular structures, respectively.

The design principle of the achromatic metalens is based on tailoring phases to compensate the dispersion, which ignores the polarization conversion efficiency to some extent. Therefore, achieving a high-efficiency achromatic metalens is an urgent issue that must be resolved. Although we have numerically demon-

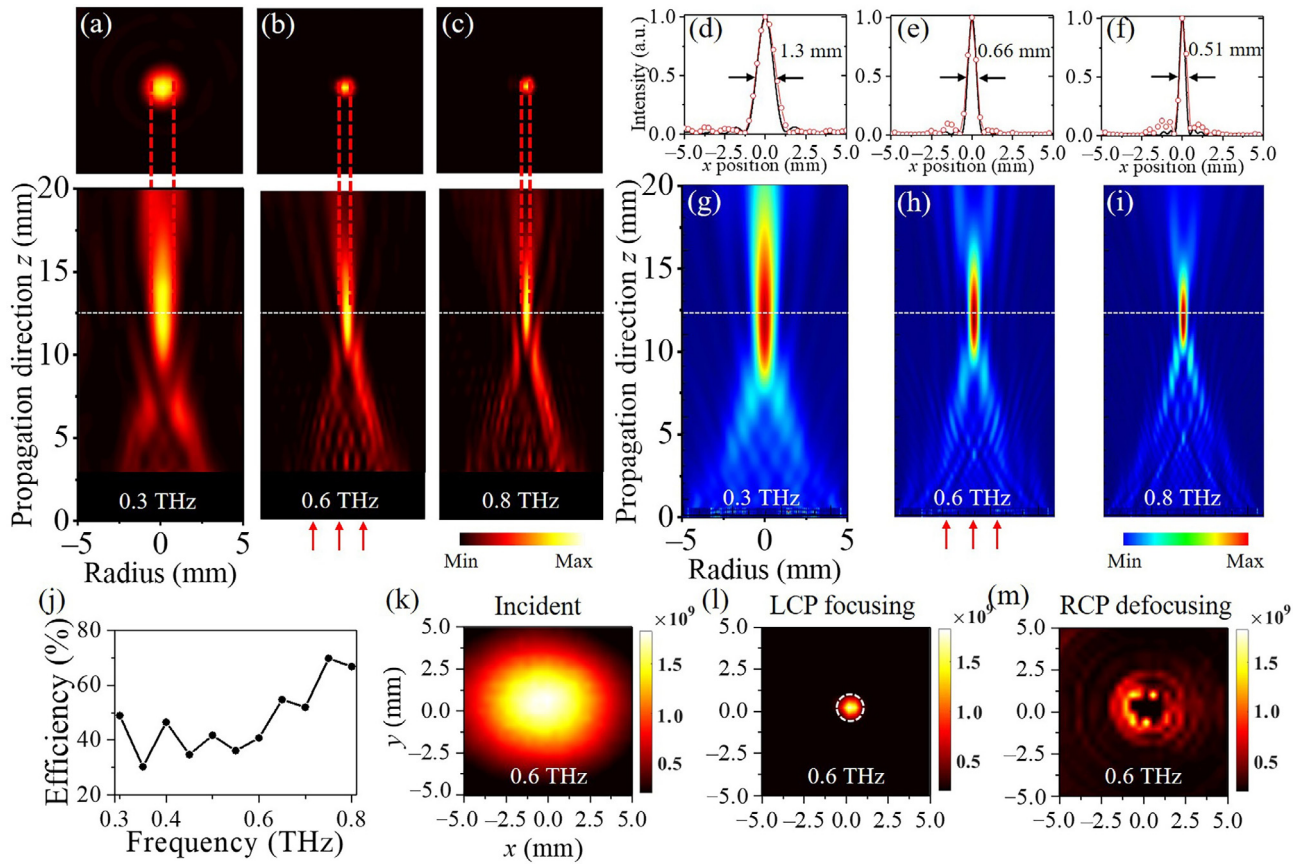


Fig. 4. (Color online) Characterization of the focusing effects for terahertz achromatic metalens based on C-shaped unit elements. (a)–(c) Horizontal and vertical cross-sections of the intensity distributions at the focal plane for the frequencies of 0.3, 0.6 and 0.8 THz, respectively. (d)–(f) Comparison of the profiles of the focal spots between the simulation and experimental results. (g)–(i) Simulation results for frequencies of 0.3, 0.6 and 0.8 THz, respectively. (j) Efficiency of the achromatic focusing. (k)–(m) Incident, LCP focusing and RCP defocusing distribution at the frequency of 0.6 THz, respectively.

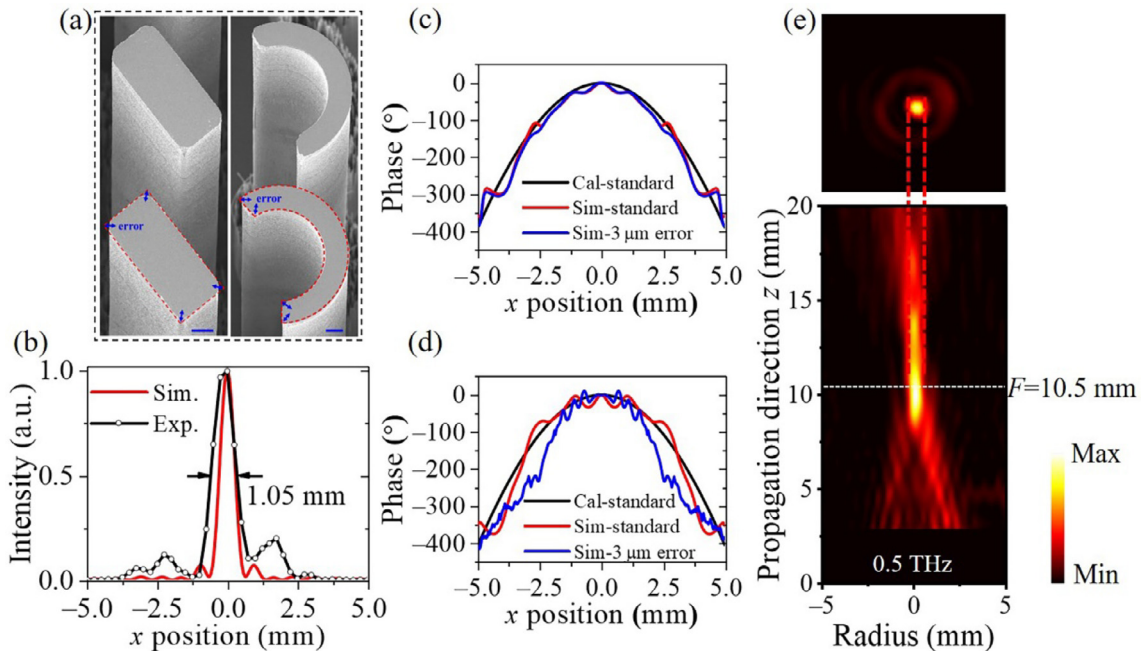


Fig. 5. (Color online) Phase distributions of the metalenses with different fabrication defects. (a) Fillet errors for the metalenses based on the rectangular and C-shaped unit, where the blue scale bar is 10 μm . (b) Comparison of the FWHM between the experimental and simulation results. (c), (d) Actual phase deviations from the ideal distributions corresponding to situations when the fillet error is 3 μm for the C-shaped and rectangular unit elements. (e) Electric field distribution along the cross-plane (x - z plane) and the focal spot distribution at $F = 10.5$ mm.

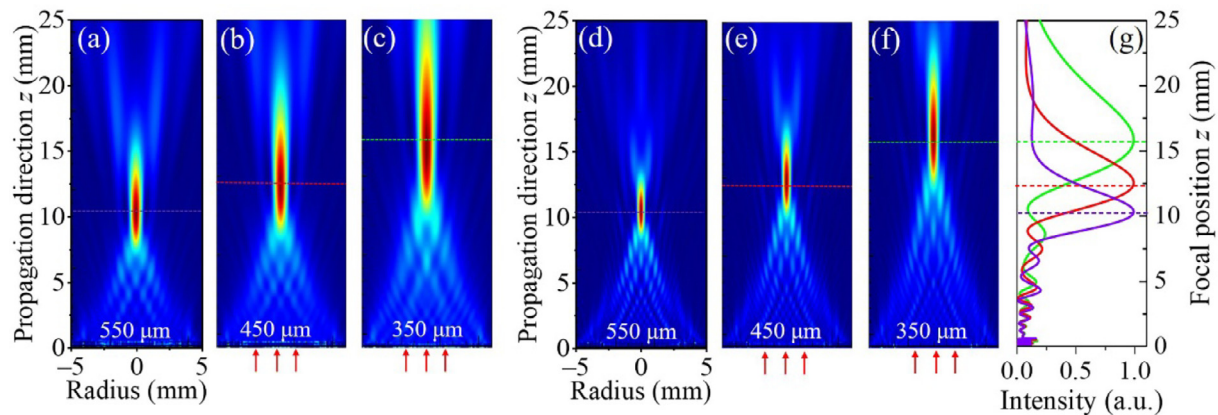


Fig. 6. (Color online) Focusing effects of the metalens with varying unit depths. Cross-section of field distributions of the metalens based on C-shaped unit elements with various depths of 550, 450 and 350 μm at frequencies of (a)–(c) 0.3 and (d)–(f) 0.8 THz, respectively. The dotted lines of each colour represent the focal length at the corresponding depths, and the lines of the same colour represent the same focal length at frequencies of 0.3 and 0.8 THz. (g) Summary of the profiles of Fig. 6a–f at frequencies of 0.3 and 0.8 THz with the etching depths of 550, 450 and 350 μm .

strated the robustness of the metalens, the fabricated sample may suffer from various problems, such as the variation in the achromatic focal lengths and other problems in engineering applications. Furthermore, as the vital limiting factor in the deep etching process is the aspect ratio, which is the main factor that causes fabrication defects, reducing the aspect ratio will be the focus of our next step.

5. Conclusion

In conclusion, a high-NA achromatic metalens based on C-shaped or rectangular unit elements has been designed by combining the resonant phase with the geometric phase, which is first reported theoretically and experimentally within a broadband terahertz frequency range. Moreover, the effects due to shape deformations and etching depth deviations are simulated separately, and the results indicate that the achromatic lens possesses a suitable robustness. The realizations of terahertz broadband achromatic focusing lenses have potential applications as metasurfaces in practical engineering for hyperspectral terahertz bio-imaging.

Conflict of interest

The authors declare that they have no conflict of interest.

Acknowledgments

This work was supported in part by the National Natural Science Foundation of China (11874266, 11604208, 61705131, and 81701745), Shanghai Science and Technology Committee of China (16ZR1445600 and 16ZR1445500), and Chen Guang Program of China (17CG49). S.W. and T.L. thank the support from National Key R&D Program of China (2017YFA0303700, 2016YFA0202103), and the National Natural Science Foundation of China (11822406, 11834007, 11674167, 11621091, 11774164, and 91850204).

Author contributions

Qingqing Cheng, Meilin Ma and Dong Yu developed the theoretical aspects and performed the numerical design and terahertz near-field measurement; Meilin Ma and Dong Yu carried out the simulation; Jingya Xie, Juncheng Wang and Nianxi Xu fabricated the samples; Dong Yu, Zhixiong Shen and Hanming Guo built-up the near-field system for measurement; Qingqing Cheng, Dong

Yu and Zhixiong Shen performed the sample preparation and data analysis; Qingqing Cheng, Dong Yu, Zhixiong Shen, Wei Hu, Shuming Wang and Tao Li analysed the data; Qingqing Cheng and Songlin Zhuang organised the project, designed the experiments, analysed the results and prepared the manuscripts. All authors discussed the results and commented on the manuscript.

Appendix A. Supplementary material

Supplementary material to this article can be found online at <https://doi.org/10.1016/j.scib.2019.08.004>.

References

- Planchon TA, Mercère P, Chériaux G, et al. Off-axis aberration compensation of focusing with spherical mirrors using deformable mirrors. *Opt Commun* 2003;216:25–31.
- Lo YH, Leonhardt R. Aspheric lenses for terahertz imaging. *Opt Express* 2008;16:15991–8.
- Yu NF, Genevet P, Kats MA, et al. Light propagation with phase discontinuities: generalized laws of reflection and refraction. *Science* 2011;334:333–7.
- Kildishev AV, Boltasseva A, Shalaev VM. Planar photonics with metasurfaces. *Science* 2013;339:1232009.
- Yu NF, Capasso F. Flat optics with designer metasurfaces. *Nat Mater* 2014;13:139–50.
- Genevet P, Capasso F, Aieta F, et al. Recent advances in planar optics: from plasmonic to dielectric metasurfaces. *Optica* 2017;4:139–52.
- Ge SJ, Chen P, Shen ZX, et al. Terahertz vortex beam generator based on a photopatterned large birefringence liquid crystal. *Opt Express* 2017;25:12349–56.
- Shen ZX, Zhou SH, Ge SJ, et al. Liquid-crystal-integrated metadevice: towards active multifunctional terahertz wave manipulations. *Opt Lett* 2018;43:4695–8.
- Zang XF, Zhu YM, Mao CX, et al. Manipulating terahertz plasmonic vortex based on geometric and dynamic phase. *Adv Opt Mater* 2019;7:1801328.
- Zhang HF, Kang M, Zhang XQ, et al. Coherent control of optical spin-to-orbital angular momentum conversion in metasurface. *Adv Mater* 2017;29:1604252.
- Ni XJ, Emani NK, Kildishev AV, et al. Broadband light bending with plasmonic nanoantennas. *Science* 2012;335:427.
- Huang LL, Chen XZ, Mühlenbernd H, et al. Dispersionless phase discontinuities for controlling light propagation. *Nano Lett* 2012;12:5750–5.
- Ding F, Wang ZX, He SL, et al. Broadband high-efficiency half-wave plate: a supercell-based plasmonic metasurface approach. *ACS Nano* 2015;9:4111–9.
- Arbabi A, Horie Y, Bagheri M, et al. Dielectric metasurfaces for complete control of phase and polarization with subwavelength spatial resolution and high transmission. *Nat Nanotechnol* 2015;10:937–43.
- Kamali SM, Arbabi E, Arbabi A, et al. Highly tunable elastic dielectric metasurface lenses. *Laser Photon Rev* 2016;10:1002–8.
- Zhang L, Zhang M, Liang HW. Realization of full control of a terahertz wave using flexible metasurfaces. *Adv Opt Mater* 2017;5:1700486.
- Zheng GX, Mühlenbernd H, Kenney M, et al. Metasurface holograms reaching 80% efficiency. *Nat Nanotechnol* 2015;10:308–12.
- Khorasaninejad M, Zhu AY, Roques-Carmes C, et al. Polarization-insensitive metalenses at visible wavelengths. *Nano Lett* 2016;16:7229–34.

- [19] Arbabi A, Arbabi E, Kamali SM, et al. Miniature optical planar camera based on a wide-angle metasurface doublet corrected for monochromatic aberrations. *Nat Commun* 2016;7:13682.
- [20] Guo YH, Pu MB, Zhao ZY, et al. Merging geometric phase and plasmon retardation phase in continuously shaped metasurfaces for arbitrary orbital angular momentum generation. *ACS Photon* 2016;3:2022–9.
- [21] Yang QL, Gu JQ, Xu YH, et al. Broadband and robust metalens with nonlinear phase profiles for efficient terahertz wave control. *Adv Opt Mater* 2017;5:1601084.
- [22] Jiang X, Chen H, Li ZY, et al. All-dielectric metalens for terahertz wave imaging. *Opt Express* 2018;26:14132–42.
- [23] Chen H, Wu Z, Li ZY, et al. Sub-wavelength tight-focusing of terahertz waves by polarization-independent high-numerical-aperture dielectric metalens. *Opt Express* 2018;26:29817–25.
- [24] Huang YJ, Pu MB, Zhang F, et al. Broadband functional metasurfaces: achieving nonlinear phase generation toward achromatic surface cloaking and lensing. *Adv Opt Mater* 2019;7:1801480.
- [25] Li Y, Li X, Pu MB, et al. Achromatic flat optical components via compensation between structure and material dispersions. *Sci Rep* 2016;6:19885.
- [26] Wang Q, Zhang XQ, Xu YH, et al. A broadband metasurface-based terahertz flat-lens array. *Adv Opt Mater* 2015;3:779–85.
- [27] Zhang HF, Zhang XQ, Xu Q, et al. High-efficiency dielectric metasurfaces for polarization-dependent terahertz wavefront manipulation. *Adv Opt Mater* 2018;6:1700773.
- [28] Pu MB, Li X, Ma XL, et al. Catenary optics for achromatic generation of perfect optical angular momentum. *Sci Adv* 2015;1:e1500396.
- [29] Arbabi E, Arbabi A, Kamali SM, et al. Multiwavelength polarization-insensitive lenses based on dielectric metasurfaces with meta-molecules. *Optica* 2016;3:628–33.
- [30] Lin DM, Holsteen AL, Maguid E, et al. Photonic multitasking interleaved Si nanoantenna phased array. *Nano Lett* 2016;16:7671–6.
- [31] Arbabi E, Arbabi A, Kamali SM, et al. Controlling the sign of chromatic dispersion in diffractive optics with dielectric metasurfaces. *Optica* 2017;4:625–32.
- [32] Aieta F, Kats MA, Genevet P, et al. Multiwavelength achromatic metasurfaces by dispersive phase compensation. *Science* 2015;347:1342–5.
- [33] Khorasaninejad M, Shi Z, Zhu AY, et al. Achromatic metalens over 60 nm bandwidth in the visible and metalens with reverse chromatic dispersion. *Nano Lett* 2017;17:1819–24.
- [34] Wang SM, Wu PC, Su V-C, et al. Broadband achromatic optical metasurface devices. *Nat Commun* 2017;8:187.
- [35] Chen WT, Zhu AY, Sanjeev V, et al. A broadband achromatic metalens for focusing and imaging in the visible. *Nat Nanotechnol* 2018;13:220–6.
- [36] Wang SM, Wu PC, Su VC, et al. A broadband achromatic metalens in the visible. *Nat Nanotechnol* 2018;13:227–32.
- [37] Sun SL, He Q, Hao JM, et al. Electromagnetic metasurfaces: physics and applications. *Adv Opt Photon* 2019;11:380–479.
- [38] Li GX. Achromatic metasurface lens at visible wavelengths. *Sci Bull* 2018;63:333–5.



Shuming Wang is an associate professor in National Laboratory of Solid State Microstructures, Nanjing University. He received his Ph.D. degree at Nanjing University in 2009. He specializes in nanophotonics, metasurfaces (metamaterials), plasmonics, and quantum optics.



Tao Li is a professor in Nanjing University (NJU). He received his Ph.D. degree at NJU in 2005, joined College of Engineering and Applied Sciences in 2008, and was promoted to full professor in 2013. His research includes plasmonics, metamaterials, and nanophotonics.



Songlin Zhuang is a professor in University of Shanghai for Science and Technology. He received his Ph.D. degree at Pennsylvania state university in 1982. His research interests are graded refractive index optical materials, theory of vector mode status and optical superresolution imaging.



Qingqing Cheng is an associate professor in University of Shanghai for Science and Technology (USST). He received his Ph.D. degree at Nanjing University in 2015, and then joined USST in 2015 and awarded the “Chenguang Scholars”. His research includes optical integrated circuits and terahertz diffraction managements.